






## Magnetic properties of an individual *Magnetospirillum gryphiswaldense* cell

Mathias M. Claus <sup>1,2</sup> Marcus Wyss <sup>1</sup> Dirk Schüler <sup>3</sup> Martino Poggio <sup>1,2</sup> and Boris Gross <sup>2</sup>

<sup>1</sup>*Swiss Nanoscience Institute, University of Basel, Klingelbergstrasse 82, 4056 Basel, Switzerland*

<sup>2</sup>*Department of Physics, University of Basel, Klingelbergstrasse 82, 4056 Basel, Switzerland*

<sup>3</sup>*Lehrstuhl für Mikrobiologie, University of Bayreuth, Universitätsstraße 30, 95447 Bayreuth, Germany*



(Received 4 March 2024; accepted 9 January 2026; published 30 January 2026)

Many bacteria share the fascinating ability to sense Earth's magnetic field—a process known as magnetotaxis. These bacteria synthesize magnetic nanoparticles, called magnetosomes, within their own cell body and arrange them to form a linear magnetic chain. The chain, which behaves like a compass needle, aligns the microorganisms with the geomagnetic field. Here, we measure the magnetic hysteresis of an individual bacterium of the species *Magnetospirillum gryphiswaldense* via ultrasensitive torque magnetometry. These measurements, in combination with transmission electron microscopy and micromagnetic simulations, reveal the magnetic configurations of the magnetosomes, their progression as a function of applied field, as well as the total remanent magnetic moment and effective magnetic anisotropy of a chain within a single bacterium. Knowledge of these properties is crucial both for understanding the mechanisms behind magnetotaxis and for the design of systems exploiting magnetotactic bacteria in biomedical applications.

DOI: [10.1103/PhysRevE.113.014408](https://doi.org/10.1103/PhysRevE.113.014408)

### I. INTRODUCTION

Nature has invented an incredible mechanism to lead magnetotactic bacteria such as *Magnetospirillum gryphiswaldense* to its optimum feeding grounds: a compass needle in its cell body in the form of a chain of self-assembled magnetite crystallites, each a few tens of nanometers in diameter [1–3]. Even better than a compass, which only indicates the direction of the Earth's magnetic field, this chain of magnetosomes directly orients the bacterium along the field, as a result of the torque exerted. Using its flagella and a biological sensor for oxygen content [4], the bacterium then propels itself along the magnetic field lines toward sources of nourishment in aquatic sediments. By restricting *M. gryph.*'s motion along one dimension, the chain of magnetosomes increases the efficiency of this search [5,6].

The discovery of magnetotactic bacteria has inspired a number of ideas for biomedical applications [7–13], including using them as nanorobots with magnetic actuation [14,15] or as sensing devices [16]. The biomineralization process governing the formation of magnetosome chains is also of great interest for finding new routes of material generation [17]. More exotic research directions include the use of magnetotactic bacteria in waste water treatment [18] or studies linking the presence of magnetite nanoparticles—similar to those making up magnetosomes—in meteorites from Mars to potential presence of ancient life on that planet [19–21].

The magnetism of a chain of magnetosomes within a single *M. gryph.* is complex: It consists of several tens of individual nanomagnets, one after another in a stringlike arrangement. Because of their small size, each magnetosome can be approximated as a single-domain magnet, whose magnetism is determined both by the cubic anisotropy of magnetite and the magnetosome's shape. The fact that each magnetosome takes an unknown orientation in space adds further

complexity. Finally—and crucially for the biological function of the chain—dipolar interactions between nearby magnetosomes result in a net preferred orientation along the chain axis. The competition between these anisotropies defines the orientation of each magnetosome's magnetic moment.

Precise measurements of the magnetic properties of magnetotactic bacteria, specifically anisotropy and total magnetic moment, are the key to understanding the mechanisms behind magnetotaxis [22–28]. One approach is to monitor the motion of either ensembles or individual bacteria in the presence of magnetic fields [29–33]. Reufer *et al.* [30] investigated the trajectories of *M. gryph.* swimming in a magnetic field, determining an average magnetic moment of  $2 \times 10^{-16} \text{ A m}^2$  per bacterium. Zahn *et al.* [29] extracted the moment of about 150 bacteria in liquid by tracking and modeling the rotation and translation of individual bacteria under the influence of magnetic tweezers. Typically, however, magnetic properties deduced from such measurements rely on assumptions about the motion of the bacteria in liquid. The magnetic moment of ensembles of magnetotactic bacteria has been measured directly using a superconducting quantum interference device (SQUID) [34,35]. Individual bacteria have also been studied via magnetic imaging techniques, including x-ray magnetic circular dichroism combined with scanning transmission x-ray microscopy [36–40] and electron holography [41]. In particular, Dunin-Borowski *et al.* used electron holography to visualize the magnetic stray fields of an individual *Magnetospirillum magnetotacticum* in remanence [41].

The magnetic hysteresis of an individual bacterium, from which magnetic properties such as coercivity, anisotropy, and switching behavior can be determined, is challenging to measure due to the tiny magnetic moment of a single chain of magnetosomes [37,42,43]. Knowledge of these properties is especially important for applications involving magnetic actuation or sensing.

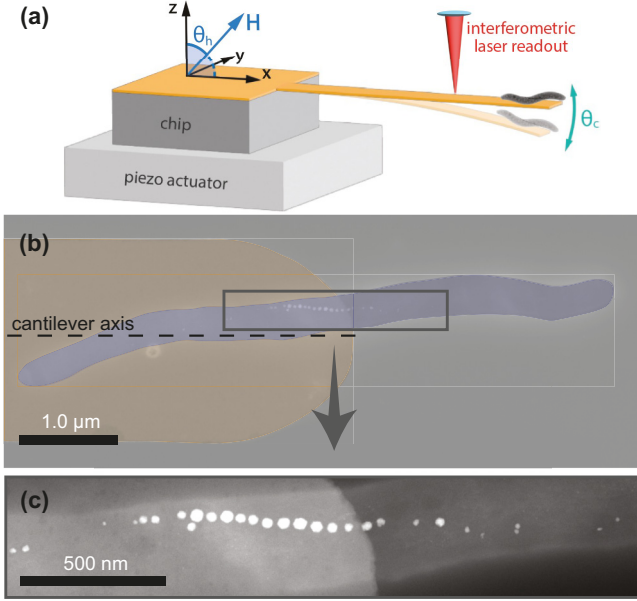


FIG. 1. Measurement setup and bacterium-on-cantilever probe. (a) Sketch of a cantilever with a single bacterium attached to the tip and definition of the coordinate axes. (b) False color high-angle annular dark-field scanning transmission electron microscopy image showing the relative orientation of the magnetosome chain with respect to the cantilever axis and (c) a close-up view of the magnetosome chain.

Dynamic cantilever magnetometry (DCM) [44–47], which is a particularly sensitive form of torque magnetometry, provides a method for measuring the magnetism of nanometer-scale magnetic systems. Gysin *et al.* first used DCM to measure the magnetic hysteresis of an ensemble of about 100 *M. gryph.*, resulting in a magnetic moment of  $5 \times 10^{-16} \text{ A m}^2$  [48] per bacterium. A few years later, using a more sensitive cantilever, the same group managed to measure the hysteresis of an individual *M. gryph.* [42], however, low signal-to-noise ratio precluded a detailed analysis of the measurements.

By attaching a single *M. gryph.* to an ultrasensitive SiN cantilever, we resolve its magnetic hysteresis via DCM. Furthermore, based on transmission electron microscopy (TEM) images, we create a micromagnetic model for the bacterium's chain of magnetosomes and compare it to DCM measurements. This comparison allows us to determine the likely progression of the magnetosomes' magnetic configurations as a function of applied field, as well as determining components of the remanent magnetization, effective anisotropy, and switching field of the bacterium. In measurements of ensembles, the properties of individual bacteria are obscured by inhomogeneity in the size, shape, and orientation of the chains of magnetosomes.

## II. DYNAMIC CANTILEVER MAGNETOMETRY

In DCM, as shown in Fig. 1, the sample under investigation is attached to the free end of a cantilever, which is driven into self-oscillation at its fundamental mechanical resonance frequency  $f$ . The measurement consists of monitoring changes in this frequency  $\Delta f = f - f_0$  as a function of a uniform

applied magnetic field  $\mathbf{H}$ , where  $f_0$  is the resonance frequency at  $H = 0$ .  $\Delta f$  reveals the curvature of the magnetic system's free energy with respect to rotations about the cantilever oscillation axis [49,50]:

$$\Delta f = \frac{f_0}{2k_0 l_{\text{eff}}^2} \left( \frac{\partial^2 E_m}{\partial \theta_c^2} \Big|_{\theta_c=0} \right).$$

$E_m$  is the magnetic energy,  $k_0$  the spring constant,  $l_{\text{eff}}$  the effective length, and  $\theta_c$  the cantilever's oscillation angle. A detailed derivation of this equation can be found in the Supplemental Material of Ref. [51]. This relation does not allow a direct link between magnetic moment and  $\Delta f$ , rather  $\Delta f$  can be intuitively understood in a thermodynamic framework [49] as an analog to magnetic susceptibility: while susceptibility quantifies the magnetic response of a sample to changes in the magnitude of  $\mathbf{H}$ ,  $\Delta f$  quantifies the response to changes in its orientation. Measurements of  $\Delta f$  are particularly useful for identifying magnetic phase transitions [49,51,52], as well as providing information on the switching, saturation magnetization, coercivity, and the anisotropy of a magnetic system [53].

The cantilevers used in this measurement are fabricated from SiN and are  $55.8 \mu\text{m}$  long,  $1.94 \mu\text{m}$  wide, and  $50 \text{ nm}$  thick. The resonance frequency  $f_0$  of the fundamental mechanical mode used for magnetometry is  $16.9 \text{ kHz}$  with an effective spring constant of  $44 \mu\text{N/m}$  and quality factor of a few thousand at room temperature. Once the sample has been attached to the end of the cantilever, the cantilever is mounted in a vibration-isolated vacuum chamber at  $10^{-6} \text{ mbar}$ . Using an external rotatable superconducting magnet, magnetic fields up to  $4.5 \text{ T}$  can be applied along any direction spanning  $225^\circ$  in the plane of cantilever oscillation ( $xz$  plane), as specified by the angle  $\theta_h$  shown in Fig. 1. The cantilever's flexural motion is read out using an optical fiber interferometer using  $100 \text{ nW}$  of laser light at  $1550 \text{ nm}$  [54]. A piezoelectric actuator mechanically drives the cantilever at  $f_0$  with a constant oscillation amplitude of a few tens of nanometers using a feedback loop implemented by a field-programmable gate array. This process enables the fast and accurate extraction of  $\Delta f$  from the cantilever deflection signal; see Appendix A.

## III. SAMPLE PREPARATION

Cells of *M. gryph.* DSM 6361 are grown under anaerobic conditions in sealed Hungate tubes containing  $10 \text{ mL}$  of flask standard medium under a headspace of  $\text{N}_2$ , as described before [55,56]. The cells are then fixed with formaldehyde. Next, a droplet of solution containing the cells is placed on the surface of a polytetrafluoroethylene sheet. A small permanent magnet placed under the sheet helps to retain bacteria, which contain magnetosomes. After  $10 \text{ min}$ , the droplet is dried with a gentle flow of compressed air. A micromanipulator system (Narishige) is used to pick up an individual bacterium from the surface, and transfer it to the free end of the ultrasoft cantilever. The bacterium is attached to the apex of the cantilever for magnetic characterization as shown in Fig. 1(b), oriented roughly with the cantilever axis using the micromanipulator, and fixed in place with UV glue (Thorlabs).

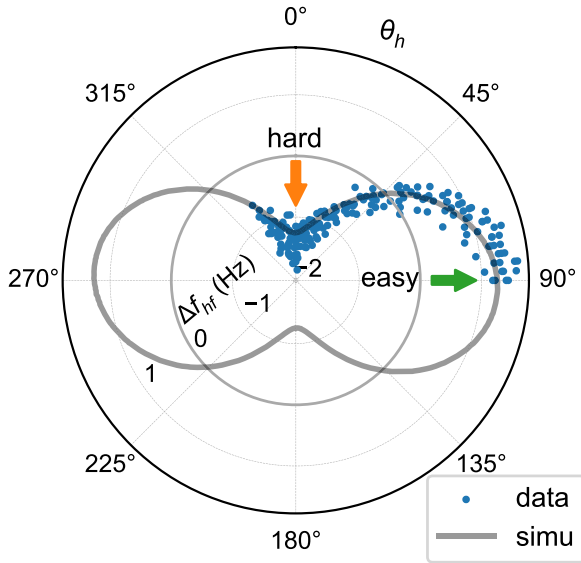


FIG. 2. DCM field rotation measurement and simulation.  $\Delta f(\theta_h)$  measured at  $\mu_0 H = 3.5$  T is plotted as blue points. Orange and green arrows indicate the hard and easy axes, respectively, as derived from simulation, shown in transparent gray.

#### IV. MEASUREMENTS

We perform two types of DCM measurements just below room temperature at  $T = 284$  K. In the first, shown in Fig. 2, we monitor  $\Delta f$  as a function of the direction  $\theta_h$  of a large field of constant magnitude  $\mu_0 H = 3.5$  T applied in the plane perpendicular to the cantilever's rotation axis ( $xz$  plane). In a magnetic field  $H$  large enough to saturate the system, as in this case, the maxima and minima of  $\Delta f(\theta_h)$  indicate the directions of the easy and hard axes, respectively [47,50]. The data plotted in Fig. 2 show the signatures of uniaxial anisotropy with the maximum and minimum separated by  $90^\circ$  and the maximum indicating the direction of the easy axis, which roughly coincides with the axis of the magnetosome chain.

In the second type of measurement, shown in Fig. 3, we measure  $\Delta f$  as we sweep  $H$  along a fixed direction from large positive to large negative values. Analysis of the resulting  $\Delta f(H)$  hysteresis measurements allows for the extraction of information on the remanent magnetic moment as well as the system's magnetic switching behavior and the progression of magnetic configurations present as the system reverses. Measurements taken for  $\theta_h = 90^\circ$  (along the axis of the magnetosome chain), shown in Figs. 3(a) and 3(b), and for  $\theta_h = 0^\circ$ , shown in Figs. 3(c) and 3(d), show the characteristic response of a magnetic system with uniaxial anisotropy with  $\mathbf{H}$  applied along its easy and hard axes, respectively [47]. The sharp discontinuity seen in Fig. 3(b) is the signature of magnetic switching in reverse applied field allowing us to deduce a coercive field of around 20 mT for the chain.

Upon completion of the DCM measurements, the cantilever is transferred to a grid for subsequent high-resolution (HR)TEM, high-angle annular dark-field scanning transmission electron microscopy (HAADF-STEM) imaging, and TEM tomography. During this process, the cantilever is broken off of its base at its clamping point, making further DCM measurements impossible. Individual magnetite magnetosomes, which are surrounded by biological tissue, are clearly resolved in the HAADF-STEM images, as shown in Fig. 1(b). This image shows the individual bacterium under investigation, which is still attached to the end of the SiN cantilever. The brightest contrast in the image corresponds to the projection of each magnetosome on the  $xy$  plane. The image reveals the alignment of the magnetosome chain with the cantilever's long axis. TEM tomography in combination with a deep learning algorithm then allows the construction of a realistic three-dimensional (3D) model of the particles, revealing their position and morphology. Details on the 3D model are provided in Appendix C, and a list of the coordinates and volumes of each magnetosome is given in Ref. [57].

HRTEM images of each individual magnetosome and their Fourier transforms also provide information on their crystallinity and orientation. Crystal planes visible in the images

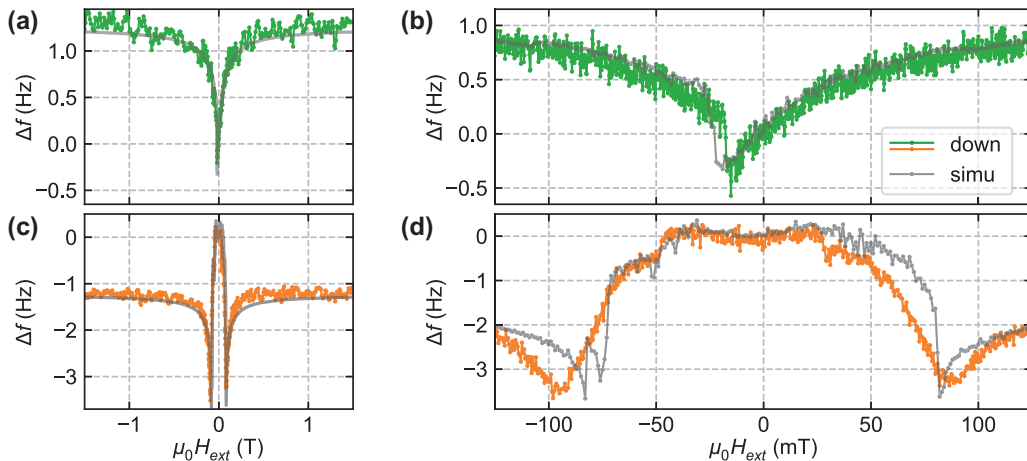


FIG. 3. DCM hysteresis as a function of applied field. (a) and (b) Measured  $\Delta f(H)$  with  $\mathbf{H}$  parallel to the magnetic easy axis plotted in green for a wide and narrow field range, respectively. (c) and (d) Measured  $\Delta f(H)$  with  $\mathbf{H}$  perpendicular to the magnetic easy axis plotted in orange, for a wide and narrow field range, respectively. In all plots, the applied field  $\mu_0 H_{\text{ext}}$  is swept from large positive values, through zero, to large negative values. Best-fit simulations are plotted in transparent gray.

show that at least 25 of the 29 magnetosomes are in a crystalline state. We do not find correlations between the orientation of these planes and either the axis of the chain or the orientation of neighboring magnetosomes [57]. Experimental circumstances prevented the extraction of the exact crystalline orientation of each magnetosome, which would have provided the orientation of each particle's magnetocrystalline anisotropy axes.

## V. ANALYSIS AND DISCUSSION

DCM data plotted in Fig. 2 indicate the presence of an effective anisotropy along the chain of magnetosomes of uniaxial character. Detailed consideration is necessary to understand the role that all the involved magnetic anisotropies play. To do so, we construct a three-dimensional, micromagnetic model of the magnetosome chain using the software package MUMAX3 [58,59]. The software solves the space and time dependent Landau-Lifshitz-Gilbert equation using a finite-difference approach, i.e., we discretize space to 1.2 nm, and determine the relaxed state of each voxel's magnetic moment in an effective magnetic field. This effective field contains all relevant interactions and anisotropy contributions: exchange interactions, dipolar interactions, cubic magnetocrystalline anisotropy of the individual particles, and an externally applied magnetic field. Ultimately, this approach allows us to precisely model the magnetic behavior of the magnetosome chain from knowledge of the position, shape, and orientation of each magnetosome as measured by TEM. Using material parameters from the literature [60], the model determines the equilibrium magnetic state of the chain for a set external magnetic field. By including the geometry of the DCM experiment and the properties of the cantilever, we calculate  $\Delta f$  and use it to iteratively adjust the input parameters, optimizing the agreement between simulated and measured  $\Delta f$ . In this way, features in hysteresis curves of  $\Delta f(H)$  such as jumps, dips, or humps can be associated with events such as magnetic switching or collective rotation of magnetic moments.

Our lack of knowledge of the orientation of the crystalline anisotropy axes of the individual magnetosomes forces us to fall back on a “best guess” strategy in order to construct a realistic model: We simulate 1000 iterations of the high-field  $\Delta f(\theta_h)$  measurement shown in Fig. 2 with randomly oriented crystalline anisotropy axes for each magnetosome. The parameters from the 20 best matches are then used to simulate the  $\Delta f(H)$  hysteresis measurements shown in Fig. 3 for a number of magnetic field orientations close to the experimental orientations. Further details on the simulations can be found in Appendix C2.

One set of parameters is found to provide the best match to the measurements, coinciding with both the experimental  $\Delta f(\theta_h)$  and  $\Delta f(H)$  data within the measurement noise, as shown in Figs. 2 and 3. The model allows the extraction of an effective uniaxial anisotropy constant for the chain as a whole, containing all contributions from the included anisotropies,  $K_u = 12.5 \text{ kJ/m}^3$ . This is in excellent agreement with the value obtained in Ref. [43] for a chain of noninteracting magnetic dipoles. Note, however, that the model therein incorporates cubic crystalline anisotropy with one axis aligned to

the chain axis for all magnetosomes, deviating from the model at hand. Typically, in literature [2], only a minimal magnetic moment for effective magnetotaxis is given. The effective anisotropy of the magnetosome chain is, however, an equally important quantity, because it quantifies the stability of the magnetic moment along the chain axis against perturbation.

It is interesting to note that most of the 1000 simulated high-field rotation curves do not show the characteristic shape resulting from simple uniaxial magnetic anisotropy along the chain direction, as measured for this bacterium in Fig. 2. Rather, they show a more complex angular dependence with signatures of the shape and randomly oriented crystalline anisotropies of the individual magnetosomes. This finding highlights that anisotropies of the individual magnetosomes should not be neglected, and suggests that the absence of features due to these anisotropies in the curve in Fig. 2 could be a coincidence due to the specific orientations of the magnetosomes in this chain or the result of an external process, such as the alignment of the magnetosomes during their growth in the *M. gryph.* cells. Nevertheless, even in iterations, in which the orientations of the individual magnetosomes result in more complex  $\Delta f(\theta_h)$ , the dominant easy axis is always set by the direction of the magnetosome chain. The fact that the chain axis sets the global energetic minimum of the magnetic anisotropy energy, despite the competing anisotropies of individual magnetosomes, ultimately ensures that every bacterium's body aligns along magnetic field lines.

Some previous studies report the alignment of a  $\langle 111 \rangle$ -type axis of individual magnetosomes with the chain axis for several different types of magnetotactic bacteria [43,61–63], including *M. gryph.* We tested the consistency of our measurements with such an alignment, by simulating a number of random orientations in which each magnetosome had a  $\langle 111 \rangle$ -type axis pinned along the chain direction. Under this constraint, no match to the measurements was found, with an exemplary result shown in Appendix C2. In fact, averaged over all magnetosomes, the simulation with the best match has an angle between the chain axis and the nearest  $\langle 111 \rangle$ -type axis of  $23^\circ$  with a standard deviation of  $12^\circ$ . We therefore conclude that no specific alignment of the  $\langle 111 \rangle$  axes with the chain axis is present in the measured bacterium.

Measurements of the hysteresis of  $\Delta f(H)$ , shown in Fig. 3, are taken with  $\mathbf{H}$  aligned along the magnetic easy and hard directions, as determined by the measurements shown in Fig. 2. In the limit of low fields, the component of the remanent magnetic moment parallel to the external magnetic field applied during the hysteresis cycle can be directly determined from  $\Delta f(H)$  with the knowledge of the cantilever properties [47]. We find  $M_x \approx (1.84 \pm 0.54) \times 10^{-16} \text{ A m}^2$  after  $\mathbf{H}$  is applied parallel to the chain axis, which is closely reproduced by our best-scenario micromagnetic model with  $M_x \approx 1.73 \times 10^{-16} \text{ A m}^2$ , for which the calculated  $\Delta f(H)$  is also shown in Fig. 3. The saturation magnetic moment within the model is  $2.0 \times 10^{-16} \text{ A m}^2$ . Therefore, almost the full moment is preserved along  $x$  in remanence after  $\mathbf{H}$  is applied parallel to the chain axis. After the application of perpendicular fields,  $M_z$  nearly vanishes:  $M_z \approx (0.26 \pm 0.14) \times 10^{-16} \text{ A m}^2$ . Note, however, that this measurement does not determine the remanent magnetic moment along the  $x$  or  $y$  directions. These values are consistent with the orientation of the effective anisotropy

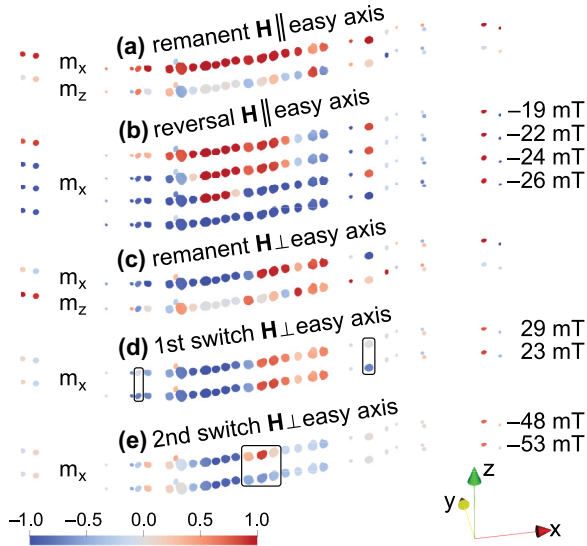


FIG. 4. Visualization of simulated magnetic states of the magnetosome chain. The color bar applies to the component of the magnetization as indicated on the left of each of the visualizations.

along the chain axis. Further, the magnitude of the saturation moment is in very good agreement with previous measurements done via optical microscopy [29,30] and DCM [48].

Further insight can be deduced from a detailed analysis of the measured and simulated  $\Delta f(H)$  shown in Fig. 3. In the measurement with the field applied along the easy axis, shown in Fig. 3(b),  $\Delta f(H)$  monotonically decreases from high fields down to zero. In a reverse field of  $-17$  mT, a jump occurs and, thereafter, the curve progresses symmetrically as for positive fields. Such behavior and the V shape of the curve can be explained via a single macrospin approximation [47]: all magnetic moments are aligned with the external field, coinciding with the easy axis of the effective magnetic anisotropy and, shortly after field reversal, collectively flip their direction in a single switching event. Simulations reveal that this picture conceals a more complex behavior: as the applied field is swept from saturation down toward zero, some magnetosomes reorient the alignment of their magnetic moments from coinciding with the chain axis to coinciding with one of their local magnetic easy axes. In the given simulation, this process proceeds in the form of a smooth rotation with decreasing magnetic field. To illustrate the result of these rotations, Fig. 4(a) shows  $m_x$  and  $m_z$  of the remanent state of the magnetosome chain, where only the main part of the chain maintains close-to-full alignment of the magnetic moments with the overall magnetic easy axis. Although the net remanent magnetic moment of the chain is nearly aligned along the chain's easy axis (only  $1.8^\circ$  off), the remanent moments of each individual magnetosome span an angle of about  $34^\circ$  with respect to this axis with a  $29^\circ$  standard deviation. This qualitatively confirms the observations of Ref. [43], in which the remanent magnetic moment of a single magnetosome was tilted away from the overall easy axis. Although the noise level of the measurement does not allow for the confirmation of related switching events or rotations of magnetic moments in the measured  $\Delta f(H)$ , the slightly reduced remanent

magnetic moment compared to the saturation moment is their direct experimental consequence. The simulations show that further sweeping  $H$  in the reverse field direction results in the full magnetic reversal of the chain via switching events of individual or a few magnetosomes, as illustrated in Fig. 4(b).

When  $H$  is applied along the magnetic hard axis, the form of the measured  $\Delta f(H)$  is consistent with a gradual rotation of all magnetic moments from alignment with  $\mathbf{H}$  toward the easy axis for decreasing  $|H|$  (compare Fig. 3(c) to Fig. 9 in Ref. [47]). The beginning of this rotation is marked by the strong dips around  $\pm 100$  mT. Deviations from this simple behavior appear in the discontinuities at  $28$  mT and  $-48$  mT in the measured  $\Delta f(H)$ . The micromagnetic simulations, which reproduce these distinctive features at nearly the same fields, suggest that they originate in an abrupt reorientation of the magnetization of individual or groups of magnetosomes, cf. Figs. 4(d) and 4(e). The discontinuity in Fig. 4(d) is connected to two individual magnetosomes in the chain reorienting its magnetization, while it corresponds in Fig. 4(e) to a switch of the magnetization of a group of three magnetosomes aligned with  $+\hat{x}$  toward  $-\hat{x}$ . More details can be found in videos included in the Supplemental Material [57]. Further switching events are either hidden in the noise of the measurement or the progression of the magnetic moments takes place slightly differently than in our best-guess simulation.

This analysis of the measurement along the magnetic hard axis also suggests a specific remanent state, as shown in Fig. 4(c). In this state, the magnetic moments on the left half of the chain orient their moments toward  $-\hat{x}$  while those on the right orient toward  $+\hat{x}$ . Together, the moments compensate each other, leading to a very low remanent moment compared to the case with  $\mathbf{H}$  applied along the easy axis. Note, however, that in other simulations, which match similarly well with experiment, this state of low remanent moment is not evident, but a state rather close to what is shown in Fig. 4(a) is observed.

As the progressions of the chain's magnetic configuration for the two different orientations of the external field show, the total magnetic moment at remanence depends strongly on the magnetic history of the chain. This dependence is a result of the relatively weak effective anisotropy, which fails to stabilize the magnetic moment in the direction of the easy axis against the application of perpendicular fields larger than several tens of millitesla. Nevertheless, because in its natural habitat *M. gryph.* likely never experiences magnetic fields of this magnitude, this effective anisotropy is sufficient to stabilize its magnetic moment in the direction of the magnetosome chain and ensure magnetotaxis. However, knowledge of the magnetic behavior for field magnitudes beyond Earth's magnetic field may become decisive for applications of magnetotactic bacteria such as biological microrobots, in which stronger fields are typically used.

## VI. CONCLUSION

Via ultrasensitive torque magnetometry, combined with transmission electron microscopy and micromagnetic simulations, we determine the remanent magnetic moment of  $(1.84 \pm 0.54) \times 10^{-16}$  A m<sup>2</sup> and a saturation moment of  $2.0 \times 10^{-16}$  A m<sup>2</sup> of an individual *M. gryph.* cell.

Furthermore, we determine an effective easy-axis anisotropy of  $12.5 \text{ kJ/m}^3$  aligned along the bacterium's chain of magnetosomes. Analysis of the magnetic hysteresis shows that this anisotropy is strong enough to stabilize the remanent magnetic moment in Earth's magnetic field. Future experiments, making use of TEM tomography and diffraction to reveal the full morphology and crystal structure of the magnetosomes [43] may allow for higher precision determination of the exact magnetic states of a single bacterium. Improved cantilever sensors could also enable the resolution of the switching of individual magnetosomes, further deepening our understanding of the magnetic reversal process. DCM measurements of many more individual bacteria would also help to determine the homogeneity of saturation moment, remanent moment, and anisotropy across a population of bacteria.

### ACKNOWLEDGMENTS

The authors thank Sascha Martin and his team in the machine shop of the Department of Physics at the University of Basel for help building the measurement system; Urs Gysin, the Nano Imaging Lab of the Swiss Nanoscience Institute, and the BioEM laboratory of the University of Basel for their support in taking TEM data. They acknowledge support from the Canton Aargau and the Swiss Nanoscience Institute's PhD program (Project No. P2107). Calculations were performed at sciCORE scientific computing center at University of Basel.

### DATA AVAILABILITY

The data that support the findings of this article are openly available [64].

### APPENDIX A: FREQUENCY MEASUREMENT

The sampling time for measurements of cantilever frequency  $f$  vary between 1 and 5 s, a time which is limited by a slow time-dependent frequency drift, which adds to the magnetic contribution,

$$f = f_0 + f_{\text{magnetic}}(H) + f_{\text{drift}}(t).$$

The drift likely originates from liquid evaporating from the bacterial cell into the surrounding vacuum. This explanation is supported by the observation that  $f$  increases monotonically in time at room temperature (the expected effect of a loss of mass on the cantilever), while no drift is observed at cryogenic temperatures, when the sample is frozen. We approximate  $f_{\text{drift}}(t)$  to be linear in time and subtract it from  $f$ . The measurement noise is close to the thermal limit of what is possible with the given setup and cantilever. For further details in  $\Delta f$  to be resolved, one would have to reduce the cantilever's mechanical dissipation and/or perform the measurements at lower temperatures.

The error of our measurement of the remanent magnetic moment is dominated by the uncertainty in determining the exact geometry of our cantilever. This uncertainty leads to a 5% error in the determination of both the cantilever's spring constant  $k_0$  and its effective length  $l_{\text{eff}}$ , ultimately affecting the uncertainty of the magnetic moment measurement. Cantilever

geometry is estimated from SEM images and goes into COMSOL simulations determining  $k_0$  and  $l_{\text{eff}}$ .

### APPENDIX B: CANTILEVER

The cantilever is commercially available (Nunano) and made of SiN. Its  $1.94 \mu\text{m}$  width and  $55.8 \mu\text{m}$  length are measured using scanning electron microscopy. Its nominal thickness is 50 nm. The experimentally observed resonance frequencies of the bacterium-loaded cantilever at zero field are  $f_0 = 16.9 \text{ kHz}$  and  $f_1 = 104.9 \text{ kHz}$ , where  $f_1$  is the frequency of the first harmonic. We use the COMSOL MULTIPHYSICS software package to construct a finite element model of the cantilever and adjust its properties so that its calculated resonance frequencies match the measured frequencies. The Young's modulus of SiN is set to 250 GPa, its density to  $3100 \text{ kg/m}^3$ , and Poisson's ratio to 0.23. The bacterium is modeled as a  $5 \mu\text{m}$  long bar with a flat bottom and rounded top. Its width is 300 nm and its density is assumed to be the same as for water ( $\rho = 1000 \text{ kg/m}^3$ ). In order to match  $f_0$  and  $f_1$ , a small, linear gradient in the thickness of the cantilever is introduced, such that it is thickest at its base (39.9 nm) and becomes thinner toward the tip (38.2 nm). Using this model, we calculate an effective length  $l_{\text{eff}} = 39.4 \mu\text{m}$  and a spring constant  $k_0 = 44 \mu\text{N/m}$  for the cantilever.

### APPENDIX C: MAGNETOSOME CHAIN

#### 1. Structural model

We use HRTEM and HAADF-STEM to image the position and morphology of each magnetosome in the chain projected onto the  $xy$  plane. We then rely on TEM tomograms to fully determine their position and shape in 3D. These tomograms, which were recorded more than a year after the original images, show a  $\sim 4\%$  increased distance between the magnetosomes. We attribute this to a deformation of the bacterium's cell body over time, and correct for this when reconstructing the morphology of the chain.

For technical reasons, we were able to reconstruct only the main part of the magnetosome chain, which contains 20 magnetosomes, via tomography. For these tomograms, we correct for the missing wedge artifact using the deep learning software package ISONET [65], which iteratively reconstructs the missing wedge information of each magnetosome. Missing wedge correction is of particular importance in the case of magnetic nanoparticles: without correction, the extracted morphology of the individual magnetosomes would show a systematic overestimation of their extent along the  $z$  axis. This effect would introduce a spurious shape anisotropy along the  $z$  axis. Note that the choice of threshold in the tomogram's intensity, which is used to set the boundary between a magnetosome and its surroundings, is chosen such that the resulting volume of the magnetosome chain yields a good match between the simulated and experimental  $\Delta f(H)$  asymptotes at high field.

For nine remote magnetosomes, which are not part of the central chain and constitute less than 5% of its total volume, we were unable to fully reconstruct their 3D position and morphology from the tomograms. We set the position of these magnetosomes along the  $z$  axis using the partial information

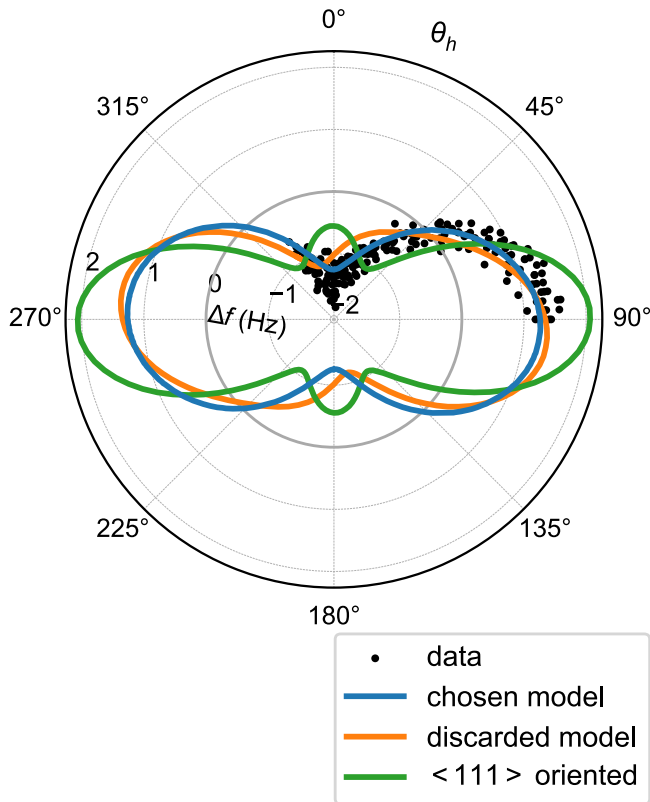


FIG. 5. DCM field rotation measurement and simulations.  $\Delta f(\theta_h)$  measured at  $\mu_0 H = 3.5$  T plotted along with various simulations with different combinations of orientations for each magnetosome's anisotropy axes.

from the tomogram combined with an extrapolation of their position in 3D based on their nearest neighbor's position and the overall shape of the chain. We further assume that their morphology is an ellipsoid of revolution, providing uniaxial anisotropy as the dominant shape anisotropy term, as shown for the magnetosomes of *M. gryph.* [61]. The unknown extent of these magnetosomes along the  $z$  axis is then set to the average of the lateral extents; see Ref. [57]. Because they constitute a small fraction of the total volume of the chain, these magnetosomes play a minor role in its magnetic behavior.

Ultimately, the procedure described above yields a 3D model of the magnetosome chain with  $\sim 1.2$  nm pixel size. A

list of all magnetosomes and their properties along with TEM images of each are provided in Ref. [57].

## 2. Micromagnetic model

Micromagnetic simulations are performed with the finite-difference software package MUMAX3. Material parameters are taken from literature at the measurement temperature  $T = 284$  K [60]: we set the exchange stiffness to  $A_{\text{ex}} = 13.5$  pJ/m, the saturation magnetization to  $M_s = 483.9$  kA/m, and the first order cubic anisotropy constant to  $K_{c1} = -14.0$  kJ/m<sup>3</sup>.

As discussed in the preceding section, the morphology and position of the individual magnetosomes in 3D space are taken from TEM data. Because the orientation of each magnetosome's cubic anisotropy axes is unknown, we simulate the magnetosome chain with many configurations of different randomly chosen orientations of each magnetosome's crystalline anisotropy axes.

The simulated configuration that best matches the DCM measurements is presented in Sec. V and is chosen via an iterative process. We start by finding the 20 best matches to the high-field measurement of  $\Delta f(\theta_h)$ , shown in Fig. 2, from  $\sim 1000$  configurations of different randomly oriented cubic anisotropy axes. The best matches are determined by minimizing the root-mean-square deviation between the simulated and measured data. For each of these 20 configurations, we then simulate five  $\Delta f(H)$  curves with the external field aligned along slightly different directions within a few degrees, which is our experimental error, of the easy (hard) axis. These small deviations are considered, because many features in the simulations depend sensitively on this alignment. Finally, we choose the configuration of magnetosome orientations, whose simulated hard- and easy-axis  $\Delta f(H)$  curves best qualitatively match both measured curves. A match is judged by taking into account how well the simulation reproduces the high-field asymptotes, curve shape, and switching events of both the easy- and hard-axis measurements. To illustrate the effect of different configurations of anisotropy axis orientations within the magnetosome chain, Fig. 5 shows the  $\Delta f(\theta_h)$  measured at  $\mu_0 H = 3.5$  T for the best match along with a model that was discarded, due to poor matching with the measurement. We also plot a configuration of the magnetosome chain, in which the  $\langle 111 \rangle$ -type axes for each magnetosome are aligned with the chain axis.

- [1] R. Uebe and D. Schüler, Magnetosome biogenesis in magnetotactic bacteria, *Nat. Rev. Microbiol.* **14**, 621 (2016).
- [2] D. Faivre and D. Schüler, Magnetotactic bacteria and magnetosomes, *Chem. Rev.* **108**, 4875 (2008).
- [3] C. T. Lefèvre and D. A. Bazylinski, Ecology, diversity, and evolution of magnetotactic bacteria, *Microbiol. Mol. Biol. Rev.* **77**, 497 (2013).
- [4] F. Popp, J. P. Armitage, and D. Schüler, Polarity of bacterial magnetotaxis is controlled by aerotaxis through a common sensory pathway, *Nat. Commun.* **5**, 5398 (2014).
- [5] R. B. Frankel, D. A. Bazylinski, M. S. Johnson, and B. L. Taylor, Magneto-aerotaxis in marine coccoid bacteria, *Biophys. J.* **73**, 994 (1997).
- [6] D. Schüler, The biomineralization of magnetosomes in *Magnetospirillum gryphiswaldense*, *Int. Microbiol.* **5**, 209 (2002).
- [7] E. Alphandéry, I. Chebbi, F. Guyot, and M. Durand-Dubief, Use of bacterial magnetosomes in the magnetic hyperthermia treatment of tumours: A review, *Int. J. Hyperthermia* **29**, 801 (2013).

- [8] D. Serantes, K. Simeonidis, M. Angelakeris, O. Chubykalo-Fesenko, M. Marciello, M. d. P. Morales, D. Baldomir, and C. Martinez-Boubeta, Multiplying magnetic hyperthermia response by nanoparticle assembling, *J. Phys. Chem. C* **118**, 5927 (2014).
- [9] O. Felfoul, M. Mohammadi, S. Taherkhani, D. de Lanauze, Y. Zhong Xu, D. Loghin, S. Essa, S. Jancik, D. Houle, M. Lafleur, L. Gaboury, M. Tabrizian, N. Kaou, M. Atkin, T. Vuong, G. Batist, N. Beauchemin, D. Radzioch, and S. Martel, Magneto-aerotactic bacteria deliver drug-containing nanoliposomes to tumour hypoxic regions, *Nat. Nanotechnol.* **11**, 941 (2016).
- [10] D. Ghosh, Y. Lee, S. Thomas, A. G. Kohli, D. S. Yun, A. M. Belcher, and K. A. Kelly, M13-templated magnetic nanoparticles for targeted *in vivo* imaging of prostate cancer, *Nat. Nanotechnol.* **7**, 677 (2012).
- [11] D. Gandia, L. Gandarias, I. Rodrigo, J. Robles-García, R. Das, E. Garaió, J. A. García, M.-H. Phan, H. Srikanth, I. Orue, J. Alonso, A. Muela, and M. L. Fernández-Gubieda, Unlocking the potential of magnetotactic bacteria as magnetic hyperthermia agents, *Small* **15**, 1902626 (2019).
- [12] A. Kraupner, D. Eberbeck, D. Heinke, R. Uebe, D. Schüler, and A. Briel, Bacterial magnetosomes – nature’s powerful contribution to MPI tracer research, *Nanoscale* **9**, 5788 (2017).
- [13] F. Mickoleit, C. Lanzloth, and D. Schüler, A versatile toolkit for controllable and highly selective multifunctionalization of bacterial magnetic nanoparticles, *Small* **16**, 1906922 (2020).
- [14] I. S. M. Khalil and S. Misra, Control of magnetotactic bacteria, in *Microbiorobotics*, 2nd ed., Micro and Nano Technologies, edited by M. Kim, A. A. Julius, and U. K. Cheang (Elsevier, Boston, 2017), Chap. 4, pp. 61–79.
- [15] S. R. Mishra, M. D. Dickey, O. D. Velev, and J. B. Tracy, Selective and directional actuation of elastomer films using chained magnetic nanoparticles, *Nanoscale* **8**, 1309 (2016).
- [16] X. Jiang, J. Feng, L. Huang, Y. Wu, B. Su, W. Yang, L. Mai, and L. Jiang, Bioinspired 1D superparamagnetic magnetite arrays with magnetic field perception, *Adv. Mater.* **28**, 6952 (2016).
- [17] D. Schüler, Genetics and cell biology of magnetosome formation in magnetotactic bacteria, *FEMS Microbiol. Rev.* **32**, 654 (2008).
- [18] H. Zheng, B. Pang, S. Li, S. Ma, J. Xu, Y. Wen, and J. Tian, Construction of recombinant magnetospirillum strains for nitrate removal from wastewater based on magnetic adsorption, *Processes* **10**, 591 (2022).
- [19] B. Arato, Z. Szányi, C. Flies, D. Schüler, R. B. Frankel, P. R. Buseck, and M. Pósfai, Crystal-size and shape distributions of magnetite from uncultured magnetotactic bacteria as a potential biomarker, *Am. Mineral.* **90**, 1233 (2005).
- [20] K. L. Thomas-Keppta, S. J. Clemett, D. A. Bazylinski, J. L. Kirschvink, D. S. McKay, S. J. Wentworth, H. Vali, E. K. Gibson, and C. S. Romanek, Magnetofossils from ancient mars: a robust biosignature in the martian meteorite ALH84001, *Appl. Environ. Microbiol.* **68**, 3663 (2002).
- [21] R. B. Frankel and P. R. Buseck, Magnetite biomineralization and ancient life on mars, *Curr. Opin. Chem. Biol.* **4**, 171 (2000).
- [22] R. B. Frankel, Magnetic guidance of organisms, *Annu. Rev. Biophys. Bioeng.* **13**, 85 (1984).
- [23] A. Kalmijn, Biophysics of geomagnetic field detection, *IEEE Trans. Magn.* **17**, 1113 (1981).
- [24] X. Zhu, X. Ge, N. Li, L.-F. Wu, C. Luo, Q. Ouyang, Y. Tu, and G. Chen, Angle sensing in magnetotaxis of *Magnetospirillum magneticum* AMB-1, *Integr. Biol.* **6**, 706 (2014).
- [25] S. Klumpp and D. Faivre, Magnetotactic bacteria, *Eur. Phys. J.: Spec. Top.* **225**, 2173 (2016).
- [26] S. Klumpp, C. T. Lefèvre, M. Bennet, and D. Faivre, Swimming with magnets: From biological organisms to synthetic devices, *Phys. Rep.* **789**, 1 (2019).
- [27] S. Mohammadinejad, D. Faivre, and S. Klumpp, Stokesian dynamics simulations of a magnetotactic bacterium, *Eur. Phys. J. E* **44**, 40 (2021).
- [28] A. Codutti, M. A. Charsooghi, E. Cerdá-Doñate, H. M. Täieb, T. Robinson, D. Faivre, and S. Klumpp, Interplay of surface interaction and magnetic torque in single-cell motion of magnetotactic bacteria in microfluidic confinement, *eLife* **11**, e71527 (2022).
- [29] C. Zahn, S. Keller, M. Toro-Nahuelpan, P. Dorscht, W. Gross, M. Laumann, S. Gekle, W. Zimmermann, D. Schüler, and H. Kress, Measurement of the magnetic moment of single *Magnetospirillum gryphiswaldense* cells by magnetic tweezers, *Sci. Rep.* **7**, 3558 (2017).
- [30] M. Reufer, R. Besseling, J. Schwarz-Linek, V. A. Martinez, A. N. Morozov, J. Arlt, D. Trubitsyn, F. B. Ward, and W. C. K. Poon, Switching of swimming modes in *Magnetospirillum gryphiswaldense*, *Biophys. J.* **106**, 37 (2014).
- [31] D. Le Sage, K. Arai, D. R. Glenn, S. J. DeVience, L. M. Pham, L. Rahn-Lee, M. D. Lukin, A. Yacoby, A. Komeili, and R. L. Walsworth, Optical magnetic imaging of living cells, *Nature (London)* **496**, 486 (2013).
- [32] R. Nadkarni, S. Barkley, and C. Fradin, A comparison of methods to measure the magnetic moment of magnetotactic bacteria through analysis of their trajectories in external magnetic fields, *PLoS ONE* **8**, e82064 (2013).
- [33] A. Bahaj, P. James, and F. Moeschler, An alternative method for the estimation of the magnetic moment of non-spherical magnetotactic bacteria, *IEEE Trans. Magn.* **32**, 5133 (1996).
- [34] Y. R. Chemla, H. L. Grossman, T. S. Lee, J. Clarke, M. Adamkiewicz, and B. B. Buchanan, A new study of bacterial motion: Superconducting quantum interference device microscopy of magnetotactic bacteria, *Biophys. J.* **76**, 3323 (1999).
- [35] R. Prozorov, T. Prozorov, S. K. Mallapragada, B. Narasimhan, T. J. Williams, and D. A. Bazylinski, Magnetic irreversibility and the Verwey transition in nanocrystalline bacterial magnetite, *Phys. Rev. B* **76**, 054406 (2007).
- [36] K. P. Lam, A. P. Hitchcock, M. Obst, J. R. Lawrence, G. D. W. Swerhone, G. G. Leppard, T. Tyliczszak, C. Karunakaran, J. Wang, K. Kaznatcheev, D. A. Bazylinski, and U. Lins, Characterizing magnetism of individual magnetosomes by x-ray magnetic circular dichroism in a scanning transmission x-ray microscope, *Chem. Geol.* **270**, 110 (2010).
- [37] L. Marcano, I. n. Orue, D. Gandia, L. Gandarias, M. Weigand, R. M. Abrudan, A. García-Prieto, A. García-Arribas, A. Muela, M. L. Fernández-Gubieda, and S. Valencia, Magnetic anisotropy of individual nanomagnets embedded in biological systems determined by axi-asymmetric x-ray transmission microscopy, *ACS Nano* **16**, 7398 (2022).
- [38] S. S. Kalirai, K. P. Lam, D. A. Bazylinski, U. Lins, and A. P. Hitchcock, Examining the chemistry and magnetism of

- magnetotactic bacterium *Candidatus Magnetovibrio blakemorei* strain MV-1 using scanning transmission x-ray microscopy, *Chem. Geol.* **300-301**, 14 (2012).
- [39] S. S. Kalirai, D. A. Bazylinski, and A. P. Hitchcock, Anomalous magnetic orientations of magnetosome chains in a magnetotactic bacterium: *Magnetovibrio blakemorei* strain MV-1, *PLoS ONE* **8**, e53368 (2013).
- [40] S. Staniland, B. Ward, A. Harrison, G. van der Laan, and N. Telling, Rapid magnetosome formation shown by real-time x-ray magnetic circular dichroism, *Proc. Natl. Acad. Sci. USA* **104**, 19524 (2007).
- [41] R. E. Dunin-Borkowski, M. R. McCartney, R. B. Frankel, D. A. Bazylinski, M. Pósfai, and P. R. Buseck, Magnetic microstructure of magnetotactic bacteria by electron holography, *Science* **282**, 1868 (1998).
- [42] M. Wasem, Atomic force microscopy of nanoparticles and biological cells, Thesis, University of Basel, 2015.
- [43] I. Orue, L. Marcano, P. Bender, A. García-Prieto, S. Valencia, M. A. Mawass, D. Gil-Cartón, D. A. Venero, D. Honecker, A. García-Arribas, L. F. Barquín, A. Muela, and M. L. Fernández-Gubieda, Configuration of the magnetosome chain: A natural magnetic nanoarchitecture, *Nanoscale* **10**, 7407 (2018).
- [44] C. Rossel, P. Bauer, D. Zech, J. Hofer, M. Willemin, and H. Keller, Active microlevers as miniature torque magnetometers, *J. Appl. Phys.* **79**, 8166 (1996).
- [45] J. G. E. Harris, D. D. Awschalom, F. Matsukura, H. Ohno, K. D. Maranowski, and A. C. Gossard, Integrated micromechanical cantilever magnetometry of  $\text{Ga}_{1-x}\text{Mn}_x\text{As}$ , *Appl. Phys. Lett.* **75**, 1140 (1999).
- [46] B. C. Stipe, H. J. Mamin, T. D. Stowe, T. W. Kenny, and D. Rugar, Magnetic dissipation and fluctuations in individual nanomagnets measured by ultrasensitive cantilever magnetometry, *Phys. Rev. Lett.* **86**, 2874 (2001).
- [47] B. Gross, D. P. Weber, D. Ruffer, A. Buchter, F. Heimbach, A. Fontcuberta i Morral, D. Grundler, and M. Poggio, Dynamic cantilever magnetometry of individual CoFeB nanotubes, *Phys. Rev. B* **93**, 064409 (2016).
- [48] U. Gysin, S. Rast, A. Aste, T. Speliotis, C. Werle, and E. Meyer, Magnetic properties of nanomagnetic and biomagnetic systems analyzed using cantilever magnetometry, *Nanotechnology* **22**, 285715 (2011).
- [49] K. A. Modic, M. D. Bachmann, B. J. Ramshaw, F. Arnold, K. R. Shirer, A. Estry, J. B. Betts, N. J. Ghimire, E. D. Bauer, M. Schmidt, M. Baenitz, E. Svanidze, R. D. McDonald, A. Shekhter, and P. J. W. Moll, Resonant torsion magnetometry in anisotropic quantum materials, *Nat. Commun.* **9**, 3975 (2018).
- [50] B. Gross, S. Philipp, E. Josten, J. Leliaert, E. Wetterskog, L. Bergström, and M. Poggio, Magnetic anisotropy of individual maghemite mesocrystals, *Phys. Rev. B* **103**, 014402 (2021).
- [51] A. Mehlin, F. Xue, D. Liang, H. F. Du, M. J. Stolt, S. Jin, M. L. Tian, and M. Poggio, Stabilized skyrmion phase detected in MnSi nanowires by dynamic cantilever magnetometry, *Nano Lett.* **15**, 4839 (2015).
- [52] B. Gross, S. Philipp, K. Geirhos, A. Mehlin, S. Bordács, V. Tsurkan, A. Leonov, I. Kézsmárki, and M. Poggio, Stability of Néel-type skyrmion lattice against oblique magnetic fields in  $\text{GaV}_4\text{S}_8$  and  $\text{GaV}_4\text{Se}_8$ , *Phys. Rev. B* **102**, 104407 (2020).
- [53] S. Philipp, B. Gross, M. Reginka, M. Merkel, M. M. Claus, M. Sulliger, A. Ehresmann, and M. Poggio, Magnetic hysteresis of individual Janus particles with hemispherical exchange biased caps, *Appl. Phys. Lett.* **119**, 222406 (2021).
- [54] D. Rugar, Improved fiber-optic interferometer for atomic force microscopy, *Appl. Phys. Lett.* **55**, 2588 (1989).
- [55] U. Heyen and D. Schüler, Growth and magnetosome formation by microaerophilic *Magnetospirillum* strains in an oxygen-controlled fermentor, *Appl. Microbiol. Biotechnol.* **61**, 536 (2003).
- [56] Y. Li, E. Katzmann, S. Borg, and D. Schüler, The periplasmic nitrate reductase nap is required for anaerobic growth and involved in redox control of magnetite biomineralization in *Magnetospirillum gryphiswaldense*, *J. Bacteriol.* **194**, 4847 (2012).
- [57] See Supplemental Material at <http://link.aps.org/supplemental/10.1103/lffn-17m6> for videos showing simulations of the magnetization reversal described in Fig. 4, the properties of all measured magnetosomes, and TEM images of each.
- [58] A. Vansteenkiste, J. Leliaert, M. Dvornik, M. Helsen, F. Garcia-Sanchez, and B. Van Waeyenberge, The design and verification of MuMax3, *AIP Adv.* **4**, 107133 (2014).
- [59] L. Exl, S. Bance, F. Reichel, T. Schrefl, H. Peter Stimming, and N. J. Mauser, LaBonte's method revisited: An effective steepest descent method for micromagnetic energy minimization, *J. Appl. Phys.* **115**, 17D118 (2014).
- [60] P. Ó Conbhuí, W. Williams, K. Fabian, P. Ridley, L. Nagy, and A. R. Muxworthy, MERRILL: Micromagnetic earth related robust interpreted language laboratory, *Geochem. Geophys. Geosyst.* **19**, 1080 (2018).
- [61] D. Gandia, L. Gandarias, L. Marcano, I. n. Orue, D. Gil-Cartón, J. Alonso, A. García-Arribas, A. Muela, and M. L. Fernández-Gubieda, Elucidating the role of shape anisotropy in faceted magnetic nanoparticles using biogenic magnetosomes as a model, *Nanoscale* **12**, 16081 (2020).
- [62] A. Körnig, M. Winklhofer, J. Baumgartner, T. P. Gonzalez, P. Fratzl, and D. Faivre, Magnetite crystal orientation in magnetosome chains, *Adv. Funct. Mater.* **24**, 3926 (2014).
- [63] S. Mann, R. B. Frankel, and R. P. Blakemore, Structure, morphology and crystal growth of bacterial magnetite, *Nature (London)* **310**, 405 (1984).
- [64] M. M. Claus, M. Wyss, D. Schüler, M. Poggio, and B. Gross, Data related to paper "Magnetic properties of an individual *Magnetospirillum gryphiswaldense* cell" [Data set], Zenodo (2026), doi: 10.5281/zenodo.10730902.
- [65] Y.-T. Liu, H. Zhang, H. Wang, C.-L. Tao, G.-Q. Bi, and Z. H. Zhou, Isotropic reconstruction for electron tomography with deep learning, *Nat. Commun.* **13**, 6482 (2022).